RSC Applied Interfaces

ROYAL SOCIETY OF CHEMISTRY

PAPER

View Article Online
View Journal | View Issue

Open Access Article. Published on 08 April 2026. Downloaded on 6/3/2026 4:27:37 PM.
This article is licensed under a Creative Commons Attribution-NonCommercial 3.0 Unported Licence.

Check for updates

Cite this: *RSC Appl. Interfaces*, 2026, 3, 807

Solar light driven type-II heterojunction TiO_2@ZIF-8 nanocomposite for sustainable chlorpyrifos detoxification: physicochemical insights, mineralization pathways and antibacterial performance

Subhashree Mohanty, Bibeka Nanda Marai and Sushanta Kumar Badamali *

Chlorpyrifos (CP), a persistent organophosphate pesticide, poses significant environmental and health risks, which necessitate sustainable detoxification strategies. TiO_2@ZIF-8 nanocomposite was prepared by a combined hydrothermal–ultrasonication approach and characterized using XRD, FTIR spectroscopy, Raman, XPS, FE-SEM, HR-TEM, BET, DRS, and DLS analyses and TGA to gain insights into its structural characteristics. Moreover, the interfacial charge separation was further confirmed through Mott–Schottky and EIS measurements. Photocatalytic degradation studies showed that ~90% of CP (100 mg L^{-1}) was removed within 90 min under solar light using 0.6 g L^{-1} of the catalyst. RSM–CCD optimisation resulted in 86% CP degradation at 90 mg L^{-1} of CP, 20 mg of adsorbent, and 86 min of solar light. A band energy diagram was constructed based on Tauc plot and Mott–Schottky analyses to determine the VB and CB positions of ZIF-8, TiO_2, and TiO_2@ZIF-8, indicating the probable formation of a type-II heterojunction, which facilitated efficient charge-carrier separation, broadened the light-absorption range, and suppressed electron–hole recombination. The kinetic analysis revealed that the degradation process followed pseudo-first-order kinetics. Radical scavenging study confirmed that holes, superoxide radicals, and hydroxyl radicals were the preferentially active reactive species in the system. A plausible degradation mechanism was proposed accordingly. The composite exhibited excellent reusability by maintaining ~85% activity over four cycles. The nanocomposite demonstrated significant antibacterial efficacy against *Staphylococcus aureus* and *Escherichia coli*, suggesting multifunctional applicability in water purification. These results demonstrate that the TiO_2@ZIF-8 nanocomposite possesses both photocatalytic and antibacterial capabilities independently, enabling its potential for multifunctional applications in the future.

Received 26th December 2025,
Accepted 2nd March 2026

DOI: 10.1039/d5lf00405e

rsc.li/RSCApplInter

1. Introduction

The rapid expansion of global industrialization and agricultural sectors has raised significant concerns regarding environmental pollution. It has not only intensified the volume of pollutants entering ecosystems but also diversified their chemical complexity by deteriorating the water quality and public health. Among such pollutants, pesticides pose a critical threat due to their pervasive use, environmental persistence, and neurotoxic effects on ecosystems. Agricultural runoff, industrial effluents, and improper waste disposal have further dispersed these hazardous chemicals into water systems. Consequently, ensuring access to safe drinking water has become increasingly challenging, as the economic and technical complexities of purifying such contaminated water remain unresolved.[1]

Among the myriads of pesticides, organophosphorus pesticides (OPPs) particularly pose severe ecological and public health risks arising from their persistence, bioaccumulation potential, and carcinogenic properties. Among them, chlorpyrifos (CP), a widely used insecticide, exemplifies this crisis. Initially patented in 1966, CP has been extensively applied in agriculture, urban pest control, and household settings.[2] The detectable residues of CP are found in 89% of global surface water samples, with contaminations found up to 24 km from the application sites.[2] Its half-life in aquatic environments ranges from 30 to 120 days, allowing bioaccumulation in aquatic organisms and biomagnification through food chains. It is linked to oxidative DNA damage, chronic poisoning, acute developmental disorders, and endocrine disruption in humans, even at trace concentrations. Despite its efficacy against pests, CP is

Department of Chemistry, Utkal University, Vani Vihar, Bhubaneswar-751004, Odisha, India. E-mail: skbuche@utkaluniversity.ac.in

© 2026 The Author(s). Published by the Royal Society of Chemistry

Open Access Article. Published on 08 April 2026. Downloaded on 6/3/2026 4:27:37 PM. This article is licensed under a Creative Commons Attribution-NonCommercial 3.0 Unported Licence.

classified by the WHO as a class II hazardous chemical.[3] Its residues are frequently detected in surface waters worldwide, and the metabolites, such as chlorpyrifos-oxon and 3,5,6-trichloro-2-pyridinol (TCP), are more toxic and tenacious. In addition to these, several risks associated with CP and its contaminated aquatic sources have become an urgent priority to develop efficient and sustainable technologies to protect the environment.[4,5]

Various methods, including oxidative degradation, electrochemical treatment, adsorption, and photodegradation, have been explored for removing pollutants from aqueous solutions. However, conventional treatment methods, such as adsorption and phase-transfer processes, often fail to achieve complete degradation as they merely relocate contaminants rather than eliminating them.[6] Among these, photocatalytic degradation stands out as a mostly favourable approach owing to its simplicity, rapid degradation rates, and ability to mineralize pollutants. This process utilizes UV-visible light or sunlight to activate a semiconductor photocatalyst, generating highly reactive hydroxyl radicals (OH·) and superoxide radicals that mineralize organic contaminants into harmless by-products, eventually producing CO_2 and H_2O.[7] Among semiconductor photocatalysts, TiO_2 remains the benchmark material because of its unique combination of physicochemical and electronic properties. Compared with other semiconductors, such as ZnO, WO_3, and CdS, TiO_2 offers enhanced light absorption, superior stability, non-toxicity, and resistance to photo corrosion, making it a relatively safe alternative for environmental applications. The anatase phase is particularly favorable for photocatalytic oxidation, as its conduction band potential (~−0.5 V *vs.* NHE) is more negative than the $O_2/\cdot O_2^-$ redox potential (−0.33 V), which facilitates efficient oxygen reduction. In addition, its highly positive valence band (+2.7 V) possesses strong oxidizing ability, facilitating the formation of hydroxyl radicals.[8] Pristine TiO_2 has a wide gap of about 3.2 eV in the anatase phase, and the absorption edge falls within the UV range, which limits visible absorption. However, it favors the rapid recombination of electron and hole pairs, which reduces the photocatalytic activity. Therefore, rational modifications, such as nanocomposite engineering, surface functionalization, and coupling with porous supports, including MOFs, are being actively explored to enhance visible-light activity, suppress recombination, and maximize their photocatalytic performance in real environmental systems.

Metal–organic frameworks (MOFs) have been developed as a group of porous materials with exceptional versatility in environmental and energy applications, particularly in adsorption and photodegradation processes. Among them, ZIF-8 (zeolitic imidazole framework-8) exhibits unique features, including a high surface area, strong chemical stability, and a sodalite-type nanoporous architecture, which enables the selective adsorption of contaminants, such as pesticides, dyes, pharmaceuticals and heavy metals.[9] More importantly, when combined with semiconductors, such as TiO_2, ZIF-8 acts as an ideal support, preventing nanoparticle agglomeration, enhancing reactant diffusion, and facilitating charge separation. Its semiconductor-like behavior and ability to form nanocomposites also enhance visible-light absorption and inhibit electron–hole recombination, thereby significantly boosting photocatalytic activity. These attributes make TiO_2/ZIF-8 heterostructures highly promising for the sustainable degradation of persistent pollutants and water purification.[10–13]

Most of the reported studies on the removal of chlorpyrifos (CP) have explored a variety of degradation processes. For instance, F. Zisti *et al.* demonstrated the use of a Fe_3O_4@SiO_2/PAEDTC@MIL-101 catalyst under UV light, achieving nearly 99% degradation of 25 mg L^{-1} of CP.[14] Hakimeh Teymourinia *et al.* reported g-C_3N_5/CdS dendrite/AgNPs nanocomposite, which degrades 95.3% of CP under visible light in 60 min.[15] Similarly, Y. Tian *et al.* reported a $CuFe_2O_4$/MIL-101(Fe) catalyst capable of degrading CP with 95% efficiency under a 300 W xenon lamp.[16] Xin Liu *et al.* have degraded ~94% of CP using bifunctional composite MOF525@BDMTp under UV-vis light for 4 h.[17] Although these results are promising, they typically require artificial light sources or complex catalyst formulation, which limit their ecological sustainability, scalability, and cost-effectiveness. The key objectives of sustainable chemistry emphasis the minimization of atom usage, cost-effective material selection, and the design of reusable heterogeneous catalysts. To address these, we design a TiO_2@ZIF-8 heterostructure by uniformly dispersing anatase TiO_2 nanoparticles onto the surface of ZIF-8 through a hydrothermal–ultrasonication method. The integration of TiO_2 with ZIF-8 fulfils the required criteria, providing cost effectiveness, ease of operation, high efficiency, recyclability, heterogeneous nature and functionality under sustainable sunlight. The surface architecture and morphology of the nanocomposite are systematically characterized and discussed in detail. The photocatalytic performance is further optimized using response surface methodology (RSM) and central composite design (CCD), which identify the most efficient conditions for CP degradation. The stability of the catalyst and the heterogeneous nature of the reaction are studied, and a plausible degradation mechanism of CP is elucidated based on GC-MS analysis. Furthermore, electrochemical analyses are employed to determine the type of heterojunction and to assess the enhanced charge-transfer dynamics, along with the migration behaviour of charge carriers. Alongside pollutant removal, the nanocomposite demonstrates significant antibacterial effects against *E. coli* and *S. aureus*, highlighting its multifunctional applicability in water detoxification and microbial control.

2. Experimental

2.1 Chemicals and reagents

Zinc nitrate hexahydrate (98%), 2-methyl imidazole (98%), titanium dioxide (anatase) nanopowder (98%), and

© 2026 The Author(s). Published by the Royal Society of Chemistry

Open Access Article. Published on 08 April 2026. Downloaded on 6/3/2026 4:27:37 PM. This article is licensed under a Creative Commons Attribution-NonCommercial 3.0 Unported Licence.

anhydrous methanol (99%) of analytical grades were supplied by Sigma Aldrich, USA. Commercial-grade chlorpyrifos (Chlorpyrifos 20% EC) was bought from the local market (Bhubaneswar, India) and used without any further treatment. All experimental procedures were carried out using double-distilled water to ensure purity.

2.2 Preparation of catalysts

2.2.1 Synthesis of ZIF-8. The fabrication of ZIF-8 was carried out *via* the hydrothermal technique reported elsewhere.[18] Initially, 0.6 g of zinc nitrate hexahydrate was dissolved in 20 mL of distilled water under stirring for 15 min to form a clear and homogeneous solution. In another beaker, 9.2 g of 2-methylimidazole (2-MeIM) was dissolved in 140 mL of deionized water and stirred for 30 min for complete dissolution. The solutions were mixed and stirred for 1 h at room temperature to allow homogeneous precursor interaction. The resulting mixture turned into a cloudy white precipitate, which was transferred into a Teflon-lined stainless-steel autoclave. Then, the mixture was hydrothermally treated at 120 °C for 6 h to promote crystallization. The resulting product was recovered by centrifugation and subsequently washed with deionized water and methanol. Subsequently, the product was dried overnight at 70 °C to obtain pure ZIF-8 as a white powder.

2.2.2 Synthesis of the TiO_2@ZIF-8 nanocomposite. The TiO_2@ZIF-8 nanocomposites were synthesized through the ultrasonication method.[19] In a typical synthesis, predetermined quantities of TiO_2 nanopowder (TiO_2 np) (5%, 10% and 20% w/w ratio) were dispersed in 10 mL of anhydrous methanol and ultrasonicated (Branson 2510, 40 kHz, 150 W) for 15 min for homogeneous dispersion. To this suspension, 100 mg of synthesized ZIF-8 was added, followed by additional ultrasonication for 30 min under identical conditions to ensure thorough mixing. The product was stirred for 2 h at ambient temperature to promote homogeneous integration. The nanocomposites were collected by vacuum filtration, washed with methanol, and dried at 70 °C for 12 h to yield the composite. Among the obtained samples, the nanocomposite containing 10% (w/w) TiO_2 exhibited superior photocatalytic performance and was therefore designated as TiO_2@ZIF-8 for subsequent studies (Fig. 1).

2.3 Characterization

The structural properties of the as-synthesized ZIF-8 and TiO_2@ZIF-8 nanocomposites were studied using powder X-ray diffraction (Bruker D8 Advanced) with Cu Kα radiation (λ = 0.1548 nm), scanning 2θ angles from 0.5° to 60° at 0.01° increments with 1 s counting time per step. Surface functional groups were observed by Fourier-transform infrared (FTIR) spectroscopy (Shimadzu). Optical properties and bandgap were measured by UV-vis diffuse reflectance spectroscopy (Agilent Cary 5000) and photoluminescence spectroscopy (Hitachi F-4600), respectively. The specific surface areas were evaluated through nitrogen adsorption–desorption isotherms measured at 77 K using a surface area analyser (Micrometrics ASAP 2020, USA) system, for which

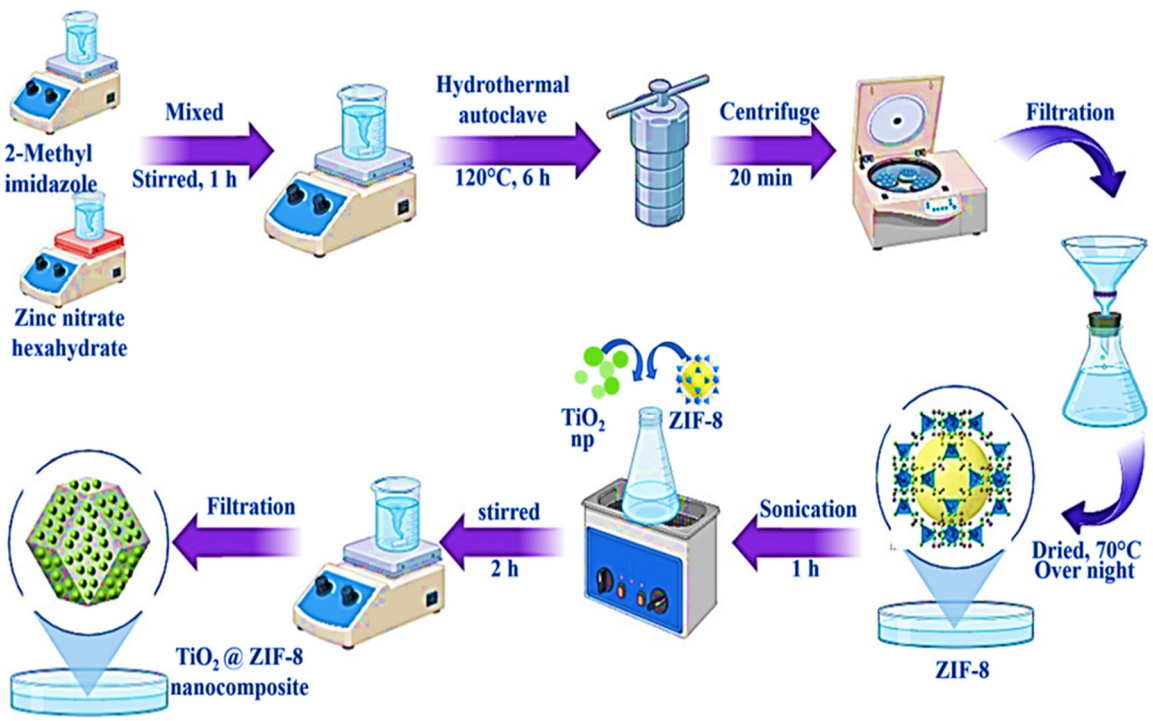

Fig. 1 Schematic presentation of TiO_2@ZIF-8 nanocomposite synthesis.

Open Access Article. Published on 08 April 2026. Downloaded on 6/3/2026 4:27:37 PM.
This article is licensed under a Creative Commons Attribution-NonCommercial 3.0 Unported Licence.

samples were degassed at 373 K for 12 h before analysis, and the Brunauer–Emmett–Teller (BET) method. Thermal stability was assessed by thermogravimetry-differential thermal analysis (STA 6000, PerkinElmer) under nitrogen atmosphere with a heating rate of 10 K min^{-1} from 300 to 1273 K. Morphological characterization was performed using field-emission scanning electron microscopy (Zeiss Auriga) coupled with energy-dispersive X-ray spectroscopy for elemental mapping. HRTEM (JEOL 2100) was used for crystallographic analysis. Surface chemical states were probed by X-ray photoelectron spectroscopy (Kratos AXIS Supra+) using monochromatic Al Kα radiation (1.48 keV). Reaction monitoring was conducted *via* UV-vis spectroscopy (Perkin Elmer, Germany) with a 1.5 nm s^{-1} scan rate. The GC-MS spectra were recorded using a Shimadzu GCMS-QP201 (Japan) system.

2.4 Experimental design

The photocatalytic degradation of chlorpyrifos (CP) using the TiO_2@ZIF-8 nanocomposite was optimized *via* response surface methodology (RSM), employing a central composite design (CCD). Three critical parameters and their ranges, as presented in Table 1, concentration (*A*), catalyst dosage (*B*), and time (*C*), were investigated for their individual and synergistic effects on degradation efficiency. The experimental design, comprising 18 randomized runs, was generated using Stat-Ease 360, with photodegradation efficiency as the response variable. A quadratic polynomial model was employed to describe the independent variables and the degradation performance. The significance of model terms and their interactions was statistically validated through analysis of variance (ANOVA), with particular emphasis on evaluating linear, quadratic, and two-factor interaction effects. Model adequacy was confirmed by comparing the coefficient of R^2 value with the adjusted R^2 value, while residual analysis and lack-of-fit tests ensured the robustness of the predictive model. This multivariate approach enabled the simultaneous optimization of multiple parameters while elucidating their complex interdependencies in the photocatalytic system.

2.5 Photocatalytic measurement

The evaluation of the photocatalytic efficiency of TiO_2@ZIF-8 was evaluated through the sunlight-driven degradation of the CP solutions. Experiments were conducted in 100 mL beakers containing 50 mL of CP solution under natural sunlight (June 2025, 20.300622° N and 85.842409°, 11:00–13:00 local time, 4.8–5.0 kWh m^{-2} day^{-1}, equivalent to an instantaneous solar intensity of ~95–100 mW cm^{-2} under clear-sky conditions) to maintain consistent light intensity. Further, 30 mg of photocatalyst was added to 100 mg L^{-1} of 50 mL CP solution and stirred in the dark for 15 min to establish adsorption–desorption equilibrium. The reaction was then employed under sunlight exposure for 90 min. The aliquots were collected at 30 min intervals for analysis. The CP degradation progress was monitored by measuring characteristic absorbance changes using UV-vis spectroscopy (λ_{max} = 300 nm), enabling the quantitative determination of the decomposition efficiency. Each experiment was carried out in triplicate using the optimized parameters determined from RSM analysis to ensure reproducibility.

Table 1 Parameters and ranges for CP removal

Independent variables			Range and levels (−1 to +1)
Factors	Code	Units	50–200
Concentration of CP	*A*	mg L^{-1}	
Catalyst dose	*B*	mg	10–50
Time	*C*	min	15–120

The degradation efficiency (%) was calculated using the following equation:

$$\text{Degradation efficiency}\ (\%) = \frac{C - C_0}{C_0} \times 100. \quad (1)$$

By applying the following equation (eqn (2)) to a pseudo-first-order kinetic model, the reaction kinetics were examined.

$$\ln\left(\frac{C}{C_0}\right) = kt, \quad (2)$$

where C is the initial concentration of CP, and C_0 is the concentration of CP after degradation.

Following the completion of the reaction, the product was isolated by the repeated extraction of the aqueous layer with diethyl ether. The combined organic extracts were dried over anhydrous magnesium sulphate, concentrated, and subsequently analyzed by GC-MS.

2.6 Photoelectrochemical measurement

Electrochemical impedance spectroscopy (EIS) and Mott–Schottky were conducted on a CHI660E electrochemical workstation (CH Instruments) using a standard three-electrode system. The TiO_2@ZIF-8 nanocomposite served as the working electrode, a saturated calomel electrode (SCE) as the reference, and a platinum sheet as the counter electrode.[17] The Mott–Schottky measurements were performed in impedance–potential mode at a fixed frequency of 1 kHz with an AC perturbation of 10 mV. EIS Nyquist plots were recorded at open-circuit potential under dark conditions in the frequency range of 10^5–10^2 Hz, using 0.5 M Na_2SO_4 aqueous solution as the electrolyte. All measurements were carried out at ambient temperature (25 ± 1 °C) after allowing the system to stabilize for 20 min.

2.7 Heterogeneity and recyclability test

The heterogeneous nature of the catalyst was evaluated using the following procedure. The catalyst was dispersed in water in the absence of the substrate and exposed to sunlight for 120 min. After this period, the suspension was filtered to separate the catalyst. The photocatalytic reactions were then

© 2026 The Author(s). Published by the Royal Society of Chemistry

Open Access Article. Published on 08 April 2026. Downloaded on 6/3/2026 4:27:37 PM. This article is licensed under a Creative Commons Attribution-NonCommercial 3.0 Unported Licence.

carried out independently using the filtrate and the recovered catalyst.

For the recycling study, the catalyst was recovered after each photocatalytic run by centrifugation, followed by filtration. After separation, the catalyst was thoroughly washed with water to eliminate any impurities, dried, and thermally regenerated. The regenerated catalyst was subsequently reused in successive degradation cycles under identical run conditions to assess its stability and reusability.

2.8 Antibacterial assessment

The antibacterial efficacy of the TiO_2@ZIF-8 nanocomposite was assessed against both Gram-negative (*E. coli*) and Gram-positive (*S. aureus*) strains. Mueller–Hinton agar (MHA) medium was prepared and aseptically poured into sterile petri plates. Overnight bacterial cultures were spread evenly across the agar surface, and wells were loaded with the ZIF-8 and TiO_2@ZIF-8 nanocomposites at concentrations of 5, 10 and 20 μg mL^{-1}. After incubation at 37 °C for 24 h, the diameters of the inhibition zones were recorded.

3. Results and discussion

3.1 Physicochemical characterizations

3.1.1 Crystallographic studies. The X-ray diffraction (XRD) patterns of pristine ZIF-8 and TiO_2@ZIF-8 nanocomposites are presented in Fig. 2(a). For ZIF-8, the characteristic diffraction peaks observed at 7.5°, 10.6°, 12.9°, 14.9°, 16.6°, 18.2°, 22.1°, 24.5°, and 26.7° corresponded to the (220), (311), (400), (422), (511), (440), (114), (233), and (044) crystallographic planes, respectively.[18,19] The sharp and well-defined peaks are indicative of the sodalite topology, high crystallinity, and phase purity of the synthesized ZIF-8 framework. In TiO_2@ZIF-8, the additional distinct peaks at 25.4°, 38.1°, 48.0°, 53.9°, and 55.1° corresponded to the (101), (112), (200), (105), and (211) planes of anatase TiO_2 (JCPDS No. 21-1272), confirming the successful incorporation of TiO_2 nanoparticles within the ZIF-8 matrix without altering its host framework.[20] Apart from that, the weak and less intense peaks at 31.6°, 34.5°, 36.2°, 46.5°, and 56.2° of the (100), (002), (101), (102), and (110) planes showed the minimal presence of hexagonal wurtzite ZnO (JCPDS No. 36-1451).[20] The crystallite sizes of ZIF-8 and TiO_2@ZIF-8 were determined using the Debye–Scherrer's equation (3),

$$D = \frac{k\lambda}{\beta \cos\theta}, \tag{3}$$

where D is the crystallite size, k is the shape factor (0.9), λ is the X-ray wavelength (1.54 Å), β is the full width at half maximum (FWHM), and θ is the Bragg's angle. The average crystallite sizes were calculated to be 45.726 and 50.073 nm for pristine ZIF-8 and TiO_2@ZIF-8, respectively. The crystallinity % was further assessed using the integration method from eqn (4):

$$\text{crystallinity\%} = \left[\frac{\text{area under crystalline peaks}}{\text{area under all peaks}}\right], \tag{4}$$

yielding 75.58% and 85.85% for ZIF-8 and TiO_2@ZIF-8 nanocomposite, respectively, confirming the high crystalline nature of both materials. This demonstrated the successful hybridization and crystallization of ZIF-8 and TiO_2@ZIF-8 nanocomposite.

3.1.2 FT IR. The FTIR spectral data of ZIF-8 and TiO_2@ZIF-8, as shown in Fig. 2(b), were analyzed to identify

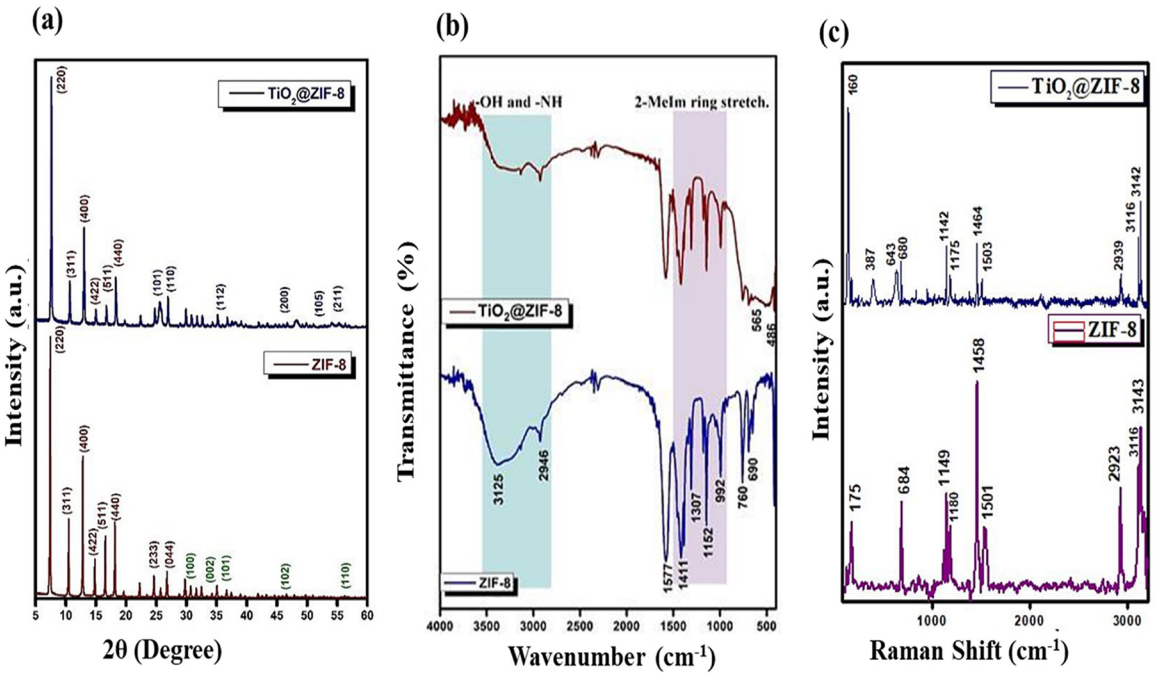

Fig. 2 (a) Powder XRD patterns, (b) FT IR spectra and (c) Raman spectra of ZIF-8 and TiO_2@ZIF-8.

Open Access Article. Published on 08 April 2026. Downloaded on 6/3/2026 4:27:37 PM.
This article is licensed under a Creative Commons Attribution-NonCommercial 3.0 Unported Licence.

the characteristic functional groups and confirm composite formation. The pristine ZIF-8 spectrum exhibited characteristic vibrations of the 2-methylimidazole linker, including C=N stretching, C–N stretching, imidazole ring bending, and a broad O–H/N–H stretching band at 1580, 1152, 760, and ~3200–3600 cm^{-1}, respectively.[18] For the TiO_2@ZIF-8 composite, these ZIF-8 signatures remained intact by preserving the ZIF-8 framework. The peaks around 800 cm^{-1} corresponded to Ti–O–Ti bridging, while new Ti–O–Ti stretching vibrations appeared around 486 cm^{-1}, confirming the TiO_2 incorporation into ZIF-8.[20] The observed slight broadening and minor shifts (~5–10 cm^{-1}) in the C=N and C–N stretching regions suggested interfacial interactions between TiO_2 nanoparticles and the ZIF-8 framework, indicating successful hybrid formation.

3.1.3 Raman analysis. The Raman spectral analysis of ZIF-8 and TiO_2@ZIF-8, as shown in Fig. 2(c), further supports the structural and composite formation. ZIF-8 displayed the characteristic peaks for Zn–N stretching, imidazole ring puckering, C–H bending and C=N stretching at 168, 686, 1147 and 1456 cm^{-1}, respectively. The high-frequency peaks at 2923 cm^{-1} were due to the aliphatic C–H stretching of the methyl group, whereas those at 3116 and 3143 cm^{-1} were attributed to the aromatic C–H stretching of the imidazole ring.[21] The TiO_2@ZIF-8 nanocomposite maintained these ZIF-8 signatures while introducing new peaks at 160 cm^{-1} (E_g), 387 cm^{-1} (B_{1g}), and 643 cm^{-1} (E_g), confirming the successful incorporation of anatase TiO_2.[19] Notably, the shifting of peaks suggested interfacial N–Ti–O bonding between ZIF-8 and TiO_2. The spectral changes demonstrated the preservation of ZIF-8, along with the interactions between TiO_2 and ZIF-8 at the interface.

3.1.4 DR-UV studies. The DR-UV spectrum, as shown in Fig. 3(a), reveals distinct optical properties for the TiO_2@ZIF-8 nanocomposite. A sharp absorption edge at 228 nm corresponded to the characteristic $\pi \rightarrow \pi^*$ transitions of ZIF-8's organic linkers, which was indicative of its wide bandgap semiconductor behaviour (Fig. S2). However, TiO_2@ZIF-8 exhibited a peak around 226 nm with enhanced visible light absorption (400–500 nm range) compared to pristine TiO_2, as evidenced by the broadening of the absorption. This extension into the visible region was further quantified by the Tauc plot (inset), which yielded a narrowed bandgap of 2.8 eV for TiO_2@ZIF-8, significantly reduced from that of pristine TiO_2 (~3.2 eV).[22] Tauc plot analysis revealed bandgap energies of 4.0 eV (ZIF-8), 3.2 eV (TiO_2), and 2.8 eV (TiO_2@ZIF-8), confirming bandgap narrowing in the composite.[18,19,22] This reduction resulted from C- and N-doping of the TiO_2 lattice by the organic ligands of ZIF-8, which introduced intermediate energy states and facilitated visible-light absorption. Additionally, the formation of Ti^{4+} ligand interactions at the interface suppressed charge recombination while further modifying the band structure. The optimized 2.8 eV bandgap enabled the production of an efficient visible-light photocatalyst.

3.1.5 Photoluminescence studies. To better investigate the charge separation characteristics of the photocatalyst material, photoluminescence (PL) spectroscopy was utilized

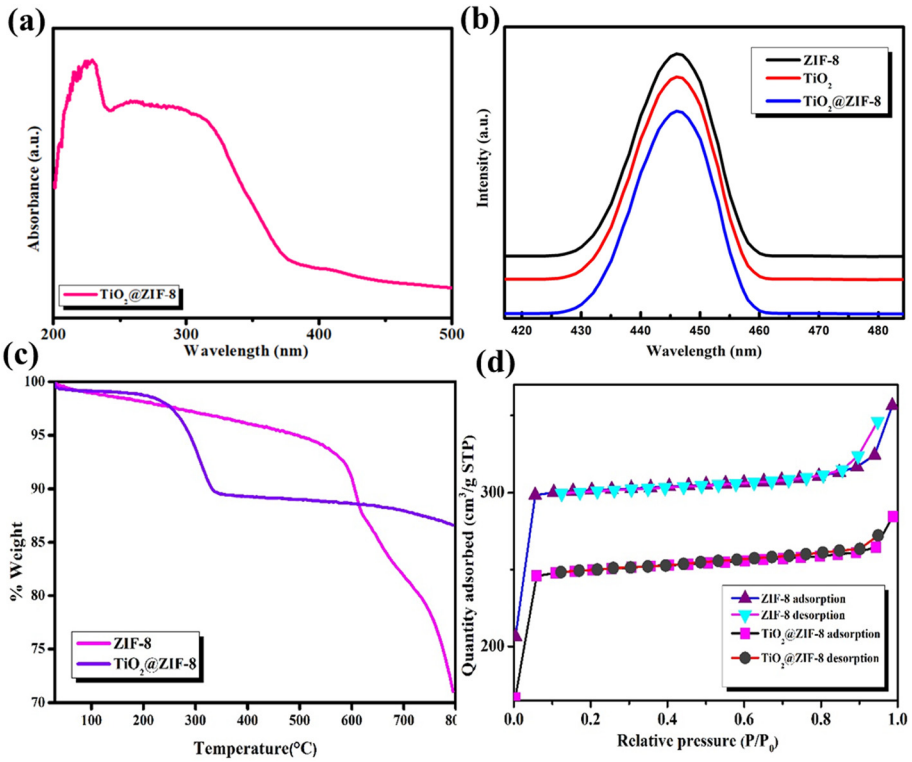

Fig. 3 (a) DR-UV spectra, (b) PL spectra, (c) TGA plot, and (d) surface area of the ZIF-8 and TiO_2@ZIF-8 nanocomposite.

© 2026 The Author(s). Published by the Royal Society of Chemistry

Open Access Article. Published on 08 April 2026. Downloaded on 6/3/2026 4:27:37 PM.
This article is licensed under a Creative Commons Attribution-NonCommercial 3.0 Unported Licence.

to analyze the recombination dynamics of photogenerated charge carriers. As illustrated in Fig. 3(b), the PL spectra provide direct insight into these processes, where strong emission intensity corresponds to high charge recombination rates. The measurements revealed that pristine ZIF-8 exhibited intense PL signals, indicating rapid electron–hole recombination. In contrast, the ZIF-8@TiO_2 composite demonstrated significantly weaker PL intensity than ZIF-8 and TiO_2 np, suggesting suppressed charge recombination. This notable reduction in PL emission strongly implied that the ZIF-8@TiO_2 nanocomposite effectively suppressed the recombination of photoinduced electron–hole pairs, likely through the establishment of enhanced charge transfer pathways between TiO_2 and ZIF-8 composites.[22]

3.1.6 TGA. The TGA plots of ZIF-8 and TiO_2@ZIF-8 revealed distinct thermal stability profiles, as shown in Fig. 3(c). For pristine ZIF-8, the decomposition occurred in two major stages due to a minor weight loss of ~9.73% below 150 °C, indicative of solvent and moisture evaporation, and a sharp weight loss of 21.85% at 300–600 °C due to the organic 2-methylimidazole linkers and collapse of the ZIF-8 framework.[23,24] The TiO_2@ZIF-8 nanocomposite exhibited an overall weight loss of only ~11.2% over the same temperature range. The relatively low weight loss of the composite was due to the overall mass loss caused by the presence of thermally stable TiO_2 nanoparticles and ZIF-8 decomposition.[22] The decomposition observed in the composite was therefore primarily attributable to the decomposition of the organic linkers in ZIF-8, while the TiO_2 matrix provided structural stability and thermal resistance. These results confirmed the enhanced thermal stability of the TiO_2@ZIF-8 nanocomposite compared with that of pristine ZIF-8.

3.1.7 N_2 adsorption–desorption studies. Among the factors influencing photocatalytic efficiency, the specific surface area

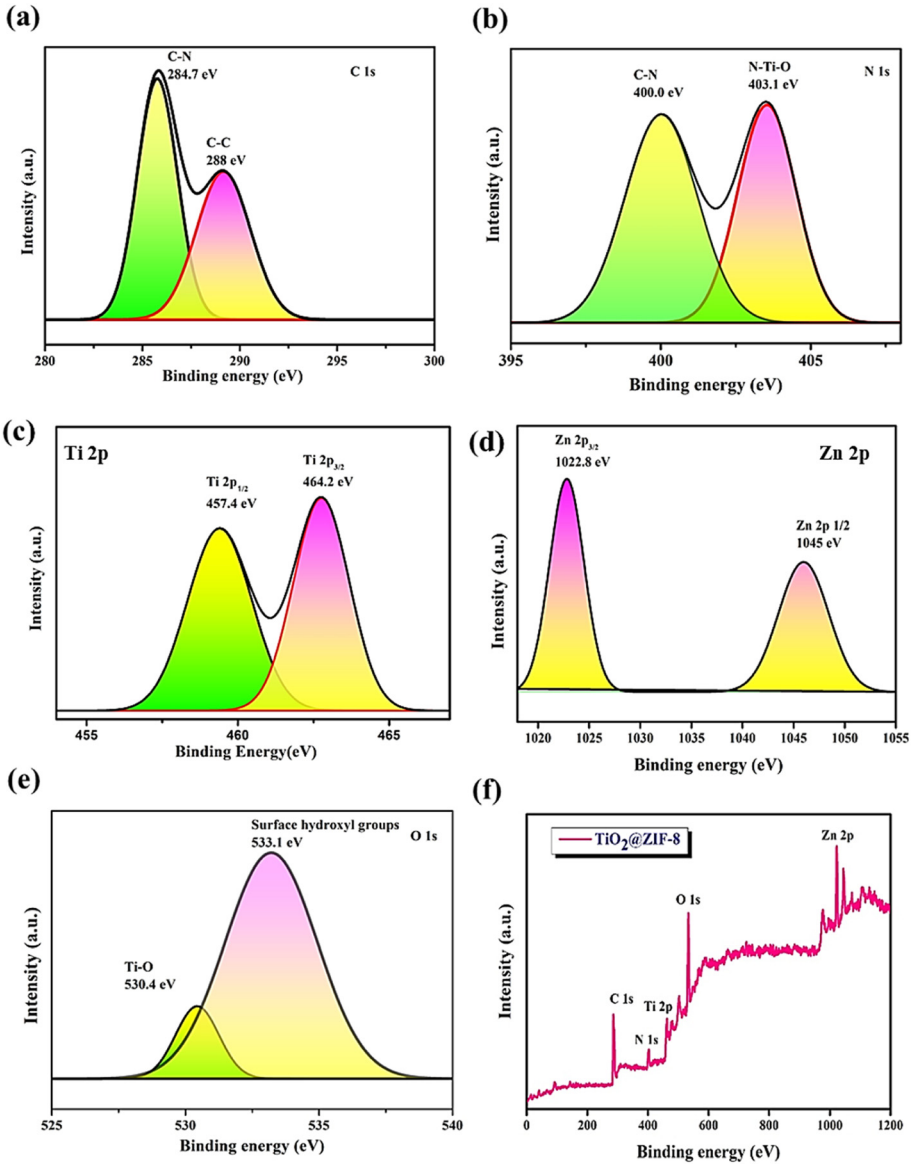

Fig. 4 High resolution XPS spectra of (a) C 1s, (b) N 1s, (c) Ti 2p, (d) Zn 2p, and (e) O 1s of TiO_2@ZIF-8. (f) XPS survey spectra of TiO_2@ZIF-8.

Open Access Article. Published on 08 April 2026. Downloaded on 6/3/2026 4:27:37 PM.
This article is licensed under a Creative Commons Attribution-NonCommercial 3.0 Unported Licence.

of the catalyst is particularly critical, as it directly influences the availability of active sites. Materials with large surface areas typically offer superior catalytic efficiency due to the high density of active centers. As shown in Fig. 3d, the N_2 adsorption–desorption isotherms of ZIF-8 and TiO_2@ZIF-8 display a combined type I/II profile in accordance with IUPAC classification, indicating the presence of a predominantly microporous framework with partial mesoporosity.[25] The adsorption at low relative pressure ($P/P_0 < 0.1$) confirmed the presence of micropores derived from the ZIF-8 lattice. Pristine ZIF-8 exhibited a high surface area, pore volume and mean pore diameter of 1153.2 $m^2\ g^{-1}$, 0.45 cc g^{-1}, and 2.7 nm, respectively. While incorporating TiO_2 nanoparticles in ZIF-8 of the TiO_2@ZIF-8 nanocomposite, these values reduced to 929 $m^2\ g^{-1}$, 0.36 cc g^{-1} and 2.5 nm, respectively. The decrease in the surface area was attributed to the surface deposition of the TiO_2 nanoparticles onto ZIF-8, which partially blocked the pore entrances and reduced nitrogen accessibility.

3.1.8 XPS analysis. XPS analysis was employed to investigate the valence states of elements in the ZIF-8@TiO_2 hybrid material. The C 1s spectrum (Fig. 4a) revealed two peaks at 284.7 eV (C–C) and 288 eV (C–N), confirming the organic structure of ZIF-8. Additionally, the N 1s spectrum (Fig. 4b) showed the peaks at 400 and 403.1 eV, which could be attributed to C–N and N–Ti–O bonding, respectively, thereby confirming the strong interfacial interaction between TiO_2 and ZIF-8. As shown in Fig. 4c, the Ti 2p spectrum displays two distinct peaks at 457.3 (Ti $2p_{3/2}$) and 464.2 eV (Ti $2p_{1/2}$), confirming the existence of Ti^{4+} in the composite. In Fig. 4d, the Zn 2p spectrum exhibits peaks at 1022.8 eV (Zn $2p_{3/2}$) and 1045.5 eV (Zn $2p_{1/2}$), indicating the preservation of Zn^{2+} in the ZIF-8 framework. The O 1s spectrum shown in Fig. 4e exhibits two peaks at 530.4 eV (lattice oxygen in anatase TiO_2) and 533.1 eV (surface hydroxyl groups), both of which play a role in photocatalysis by generating reactive oxygen species.[26,27] Taken together, these results shown in Fig. 4f, collectively determined the successful integration of TiO_2 with ZIF-8 and highlighted the electronic interactions at the nanocomposite that favoured the entire photocatalytic process.

3.1.9 FESEM. The FESEM images shown in Fig. 5 reveal the morphological features of ZIF-8 and TiO_2@ZIF-8 nanocomposite. The morphology of ZIF-8 appeared as a shape of a rhombic dodecahedron, confirming successful

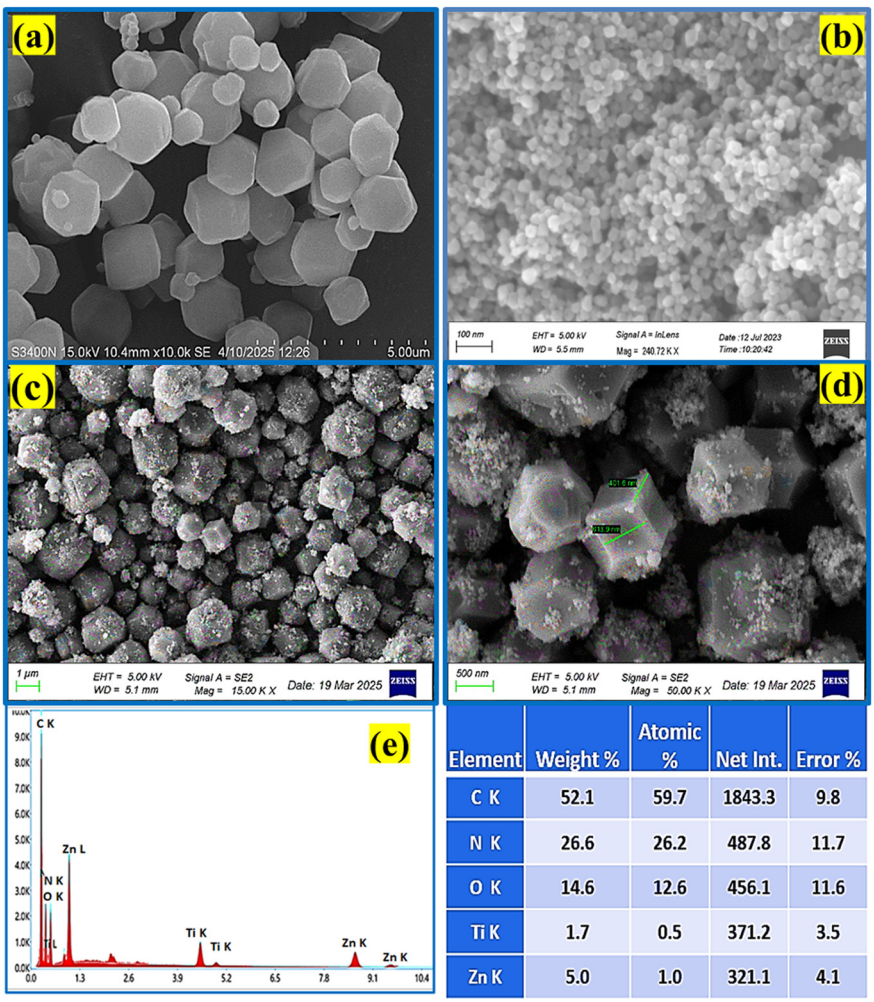

Element	Weight %	Atomic %	Net Int.	Error %
C K	52.1	59.7	1843.3	9.8
N K	26.6	26.2	487.8	11.7
O K	14.6	12.6	456.1	11.6
Ti K	1.7	0.5	371.2	3.5
Zn K	5.0	1.0	321.1	4.1

Fig. 5 FESEM images of (a) ZIF-8, (b) TiO_2 np, and (c and d) TiO_2@ZIF-8. (e) EDX mapping of TiO_2@ZIF-8.

© 2026 The Author(s). Published by the Royal Society of Chemistry

Open Access Article. Published on 08 April 2026. Downloaded on 6/3/2026 4:27:37 PM. This article is licensed under a Creative Commons Attribution-NonCommercial 3.0 Unported Licence.

crystallization.[28,29] However, the TiO_2 np displayed a spherical morphology.[22] Upon hybridization with ZIF-8, the composite showed a distinct heterostructure hybrid architecture, where the TiO_2 cores were uniformly distributed by a porous ZIF-8 framework (Fig. 5(c and d). The EDX spectrum and elemental mapping (Fig. 5(e)) confirmed the coexistence and uniform dispersal of Ti, Zn, C, O, and N in the nanocomposite, validating the integration.

3.1.10 HRTEM. High-resolution transmission electron microscopy (HRTEM) analysis was performed to investigate the morphology, crystallinity, and interfacial structure of the TiO_2@ZIF-8 nanocomposite. The HRTEM micrographs presented in Fig. 6 show that the TiO_2 nanoparticles are well dispersed and embedded within the morphology of the ZIF-8 matrix. The contrast difference between the dense TiO_2 core (darker regions) and the light ZIF-8 shell confirmed the integration of TiO_2 np into the hybrid assembly of ZIF-8. Distinct lattice spacings of ~0.28 nm (consistent with the (101) plane of anatase TiO_2) were observed on microporous ZIF-8. Selected area electron diffraction (SAED) patterns showed diffraction ring patterns of (101), (220), and (400), matching anatase TiO_2 with prominent planes, such as (101), (004), and (200), which was consistent with the XRD results.[22,30] These results confirmed that the TiO_2 nanoparticles were well-dispersed within the ZIF-8 framework while retaining crystallinity, confirming the successful formation of the TiO_2@ZIF-8 nanocomposite.

3.1.11 DLS and zeta potential. The hydrodynamic particle size of the TiO_2@ZIF-8 nanocomposite was measured by DLS in an aqueous medium, showing an average diameter of 10^3 nm. The calculated value was higher than that observed in the TEM images, which could be attributed to the fact that DLS measured the hydrodynamic diameter, including solvation layers and agglomerates in suspension, while TEM provided the particle size in the dry state. The deviation indicated a partial tendency of TiO_2@ZIF-8 to undergo agglomeration in an aqueous solution, arising from the high surface energy of unsaturated metal and imidazolate linker sites that promote particle clustering.[31]

The zeta potential of TiO_2@ZIF-8 was found to be −30 mV, suggesting moderate colloidal stability. Although this value was not significantly high enough, the negative surface charge rendered appreciable electrostatic repulsion, which helped to maintain dispersion.

3.2 Photocatalytic activity study of CP by TiO_2@ZIF-8

3.2.1 RSM–CCD-based optimization of reaction parameters. Response surface methodology (RSM) was employed to study the effects of key operational factors, such as photocatalyst dosage (*A*), CP concentration (*B*), and time (*C*), on the CP degradation efficiency in aqueous solutions. A central composite design (CCD) consisting of 18 experimental runs was utilized to model the interactions between these variables (Table S2).

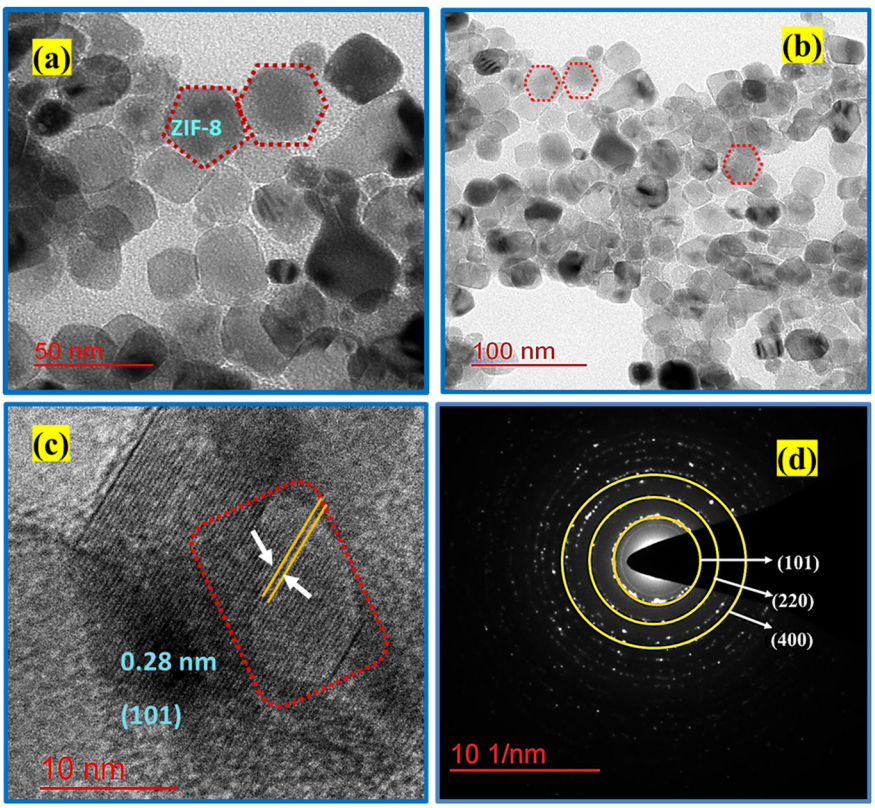

Fig. 6 HRTEM images (a–c) and SAED pattern (d) of TiO_2@ZIF-8.

Open Access Article. Published on 08 April 2026. Downloaded on 6/3/2026 4:27:37 PM.
This article is licensed under a Creative Commons Attribution-NonCommercial 3.0 Unported Licence.

$$\text{Degradation efficiency (\%)} = 78.61952 - 0.035426A + 0.291972B + 0.139493C + 0.000183AB - 0.000275AC - 0.000279BC + 0.000133A^2 - 0.004772B^2 - 0.000402C^2. \quad (5)$$

The derived quadratic regression equation (eqn (5)) revealed synergistic (positive coefficient) and antagonistic (negative coefficient) effects among the factors. The model exhibited high statistical significance, as evidenced by an F-value of 118 115.67, a P-value < 0.0001, and a large sum of squares (105.95), with significant terms including A, B, D, A^2, B^2, C^2, and D^2. Model reliability was further confirmed by a low coefficient of variation (CV = 0.0117%) and strong correlation coefficients (R^2 = 0.995, adjusted R^2 = 0.990, and predicted R^2 = 0.981). The adequate precision value (1060.54) indicated a robust signal-to-noise ratio, well above the threshold of 4, which supported the model's validity (Tables S3 and S4).[32]

Diagnostic plots were employed to evaluate the reliability of the predicted model. Fig. S5 illustrates the plot of predicted degradation efficiency against externally studentized residuals, confirming model validity as the predicted values were independent of the actual values. The random distribution of residuals within a ±4 range further supported the model's predictive accuracy. Fig. S5b displays the linear fit of externally studentized residuals against normal probability %, revealing a normally distributed linear trend that validated the model's results. The close alignment of the data points with the regression line indicated a strong correlation between actual and predicted values, validating the model's accuracy in predicting responses to variations in the independent variables. As shown in Fig. S5c, the Box–Cox plot (Fig. S5e) suggested a lambda value of 1, implying no need for response transformation in CP degradation analysis. Additionally, Cook's distance plot (Fig. S5d) showed that out of 18 experimental runs, most exhibited values near zero, indicating minimal influential outliers and robust model predictability. As shown in Fig. S5e, the actual *vs.* predicted degradation efficiency plot exhibits a strong correlation, reinforcing the model's applicability to experimental data. As shown in Fig. S5f, the externally studentized residual plot against the run number shows no discernible pattern, with residuals scattered randomly around the baseline within a ±4 range, indicating model precision and the absence of data inconsistencies.[32–34] These results collectively affirmed the model's suitability for optimizing CP degradation under the studied conditions.

3.3 Influence of operational parameters on CP degradation

The surface model 2D and 3D plots were described for the responses of different parameters as variables and one constant, through which the optimized value of CP degradation efficiency could be obtained. The plots indicated the integrated effect on the degradation of CP.

3.3.1 Effect of catalyst dose. The influence of catalyst dosage and time on the CP removal was explored, and both parameters were found to significantly impact degradation efficiency. The CP degradation efficiencies of the three different TiO_2 : ZIF-8 ratios (5%, 10%, and 20% of TiO_2) were evaluated under identical conditions, revealing efficiencies of 70%, 82% and 90%, respectively, which indicated that ZIF-8 containing 10% of TiO_2 was the best among the studied catalysts, as presented in Fig. S6a. Possibly, 5% w/w of TiO_2 may not possess sufficient active sites; on the other hand, 20% w/w of TiO_2 leads to the aggregation/blockage of active sites, as compared to the optimised 10% w/w TiO_2@ZIF-8. Hence, the optimised catalyst selected for further study was 10% w/w of TiO_2@ZIF-8. As illustrated in Fig. 7a and d, the efficiency increased with catalyst loading up to 30 mg, due to the relatively high availability of exposed active sites for CP interaction. However, increasing the dosage to 50 mg may result in light scattering, which decreases the degradation efficiency.

3.3.2 Effect of CP concentration. The concentration of CP plays a major role in the photocatalyst process, which is presented in Fig. 7(b, c, e and f). The influence of the initial CP concentration (25, 50, 100, and 200 ppm) on the photocatalytic activity of the TiO_2@ZIF-8 nanocomposite was investigated under sunlight. At low concentrations of 50 mg L^{-1}, a relatively high degradation efficiency of up to ~95% was achieved, while increasing the CP concentration up to 250 mg L^{-1} resulted in a gradual decline in photocatalytic removal. This is because, at high concentrations, more CP molecules compete for the limited active sites on the catalyst surface, thereby suppressing the generation of reactive oxygen species ($O_2\cdot^-$, OH·) responsible for pollutant degradation. In addition, high pollutant concentrations raise the turbidity of the solution, which moderates the penetration of incident photons and limits light absorption by the catalyst. Consequently, the optimum removal of CP was achieved at an initial concentration of 100 mg L^{-1} with 30 mg of the TiO_2@ZIF-8 photocatalyst at a natural pH (5.6) under 90 min of sunlight, and this condition was selected for later studies.

3.3.3 Effect of time. Time of exposure majorly influences the photocatalytic degradation of CP, as evidenced by the 3D response surface model (RSM) shown in Fig. 7(a, c and d). Its interaction with the initial CP concentration and adsorbent dosage significantly influenced degradation efficiency. As time increased (above 90 min), degradation efficiency gradually decreased. The 3D response surface model (RSM) analysis revealed that time significantly influenced the photocatalytic degradation of CP under sunlight, with its effects being closely dependent on both the initial CP concentration and adsorbent dosage.

The decrease in the degradation activity was mainly attributed to competitive adsorption and the light-shielding effect, which limited the photon penetration and reduced the

© 2026 The Author(s). Published by the Royal Society of Chemistry

Open Access Article. Published on 08 April 2026. Downloaded on 6/3/2026 4:27:37 PM.
This article is licensed under a Creative Commons Attribution-NonCommercial 3.0 Unported Licence.

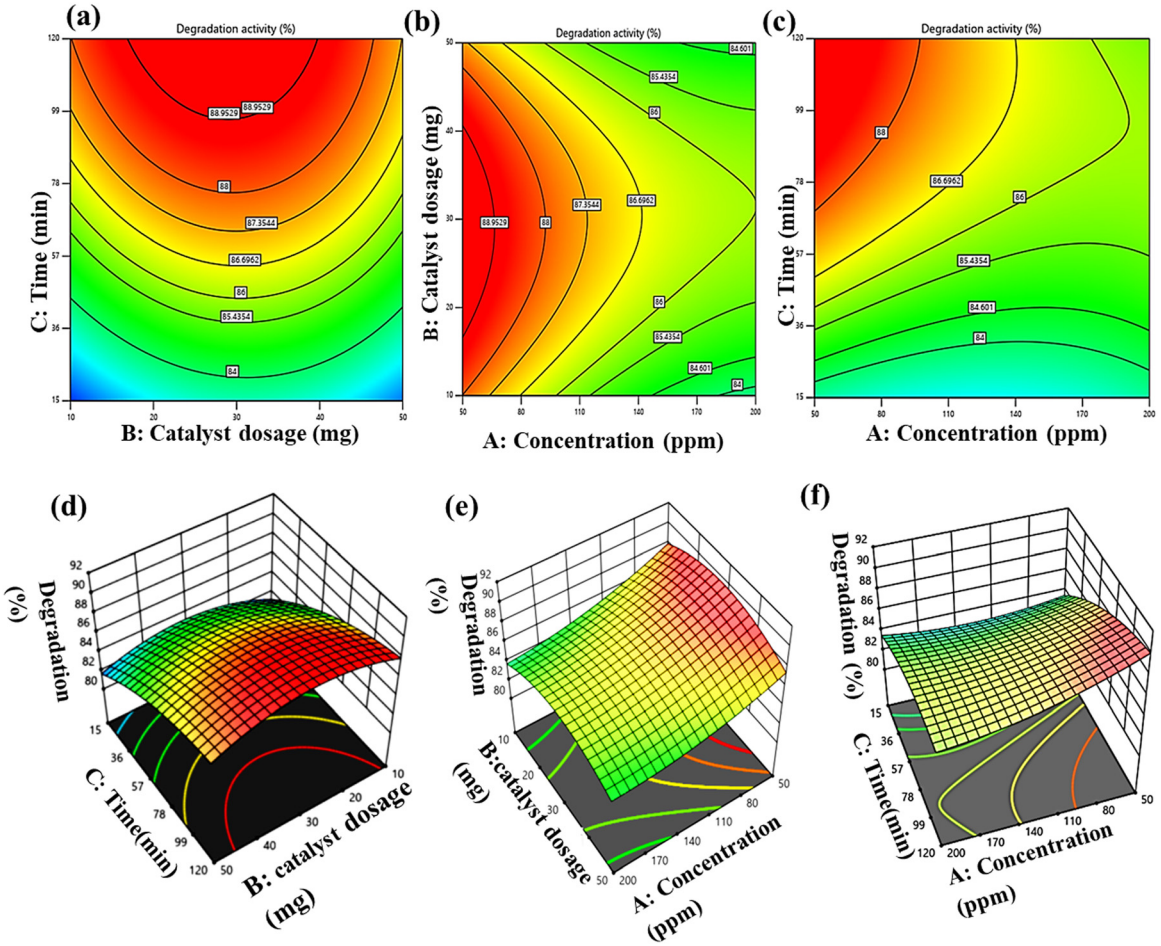

Fig. 7 Surface and three-dimensional graph of CP removal (a and d), time and dosage of catalyst (b and e), concentration of CP and dosage of catalyst (c and f), and time and concentration of CP.

availability of reactive oxygen species. Deviations from the optimized conditions led to reduced performance, arising from incomplete degradation at short times, ROS depletion at high pollutant concentrations, or light scattering at excessive catalyst loadings, highlighting the critical interdependence of these parameters in solar-driven photocatalytic systems.

3.3.4 Verification of the model. The model was validated through experiments performed in triplicate and repeated three times under the optimized conditions. The photocatalytic performances of ZIF-8, TiO_2, and TiO_2@ZIF-8 composites were assessed by monitoring the degradation of CP under sunlight. The CP degradation efficiency was in the following order: TiO_2@ZIF-8 > TiO_2 np > ZIF-8. Notably, TiO_2@ZIF-8 achieved a removal efficiency of ~90% for an optimal concentration of 100 mg L^{-1} CP with 30 mg of catalyst within 90 min under sunlight. The comparison between predicted and experimental results (Table S5) showed minor deviations, confirming the high reliability and accuracy of the model. The 3D RSM plots clearly identified the synergistic optimum at 90 ppm CP, 20 mg of adsorbent, and 86 min of exposure under sunlight, where balanced adsorption capacity with photocatalytic efficiency of 86% was achieved (Table 2).

3.4 Kinetics of the photocatalytic degradation of CP

To further investigate the reaction kinetics, $\ln(C/C_0)$ was plotted as a function of time under varying CP concentrations

Table 2 Predicted and experimental results of chlorpyrifos degradation efficiency

Pesticides	Variable	Before	After	Degradation efficiency (%)	
				Predicted	Experimental
Chlorpyrifos	Concentration (ppm)	100	90	86	90
	Weight of the adsorbent (mg)	30	20		
	Time (min)	90	86		

Open Access Article. Published on 08 April 2026. Downloaded on 6/3/2026 4:27:37 PM.
This article is licensed under a Creative Commons Attribution-NonCommercial 3.0 Unported Licence.

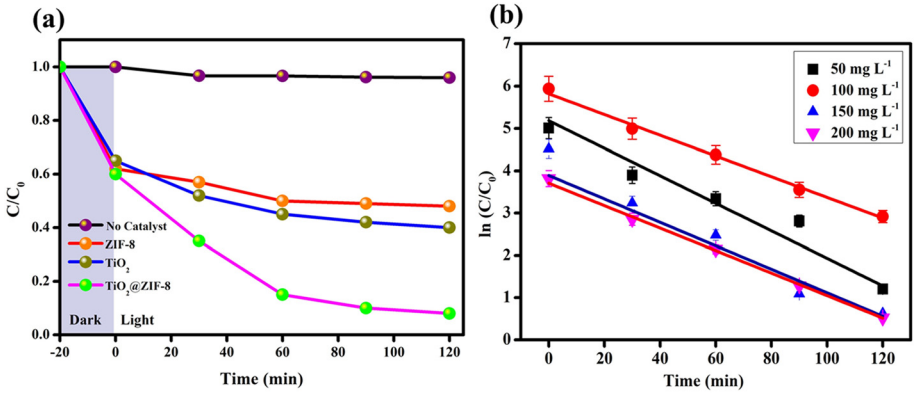

Fig. 8 Photocatalytic degradation of CP by (a) different photocatalysts and (b) kinetic study (catalyst amount: 30 mg; CP concentration: 100 mg L^{-1}, time: 120 min).

(50–200 mg L^{-1}). The linear fit of $\ln(C/C_0) = kt + b$ confirmed that the degradation followed pseudo-first-order kinetics. The rate constant (k) was 0.025 s^{-1}, and the R^2 value was 0.991 for 100 mg L^{-1} of CP by TiO_2@ZIF-8, which was the highest among all the concentrations (Fig. 8b and Table S7). This indicated that at this concentration, the balance of active site availability on the reaction surface and accessibility of CP molecules was optimal, thereby facilitating the efficient generation and utilization of reactive oxygen species (ROS).[36] At relatively low CP concentrations, the reduced pollutant availability may limit the interaction with photo-induced charge carriers, while at high concentrations, the excessive adsorption of CP molecules could lead to surface saturation and light-shielding effects, ultimately suppressing photocatalytic efficiency.[35] The observed rate constant trend was in excellent agreement with the photocatalytic performance results presented in Table S6, validating the superior efficiency of TiO_2@ZIF-8 in driving the solar-light-assisted degradation of CP.

3.5 Electrochemical study

As shown in Fig. 9a and b, the positive slopes of the Mott–Schottky plots for ZIF-8 and TiO_2 indicate their classification as n-type semiconductors. The flat-band potentials (E_{x6}) were estimated to be −1.31 and −0.43 eV for ZIF-8 and TiO_2, respectively. The negative flat-band potential of ZIF-8 suggests a higher Fermi level compared with that of TiO_2, facilitating efficient electron transfer at the TiO_2@ZIF-8 nanocomposite.[37] This alignment promoted the separation of photo-induced charge carriers under sunlight, improving photocatalysis. Similarly, EIS Nyquist plots (S8) revealed distinct charge-transfer resistance (R_{et}) for each material. ZIF-8 and TiO_2 displayed relatively large semicircular arcs, indicative of high interfacial resistance and slow charge transfer kinetics.[37] In contrast, the TiO_2@ZIF-8 composite exhibited a significantly small arc radius, demonstrating reduced charge-transfer resistance due to the synergistic interaction within the heterostructure. This improvement confirmed enhanced electron–hole separation and interfacial charge migration, which were critical for the photocatalytic degradation of CP.

3.6 Scavenger study

To identify the major reactive species involved in the photocatalytic removal of CP, various scavengers, such as potassium iodide (KI), benzoquinone (BQ), sodium oxalate ($Na_2C_2O_4$), and isopropanol (IPA), were employed for radical trapping experiments for surface ·OH, h^+, $\cdot O_2^-$, and ·OH,

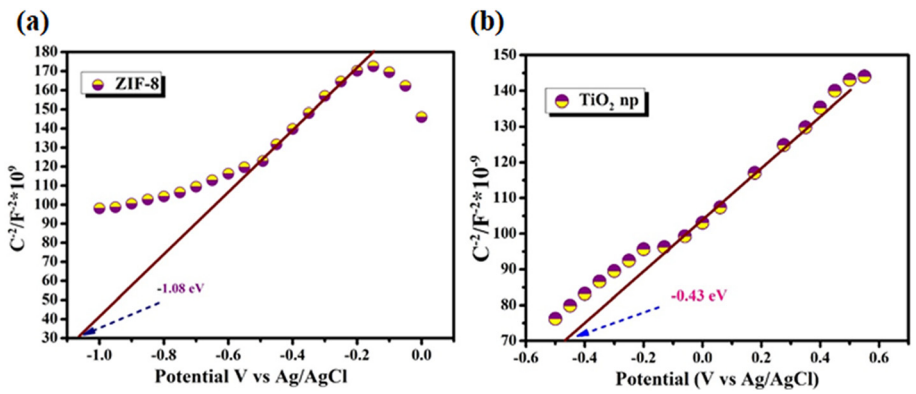

Fig. 9 Mott–Schottky plot of ZIF-8 (a) and TiO_2 np (b).

© 2026 The Author(s). Published by the Royal Society of Chemistry

Open Access Article. Published on 08 April 2026. Downloaded on 6/3/2026 4:27:37 PM.
This article is licensed under a Creative Commons Attribution-NonCommercial 3.0 Unported Licence.

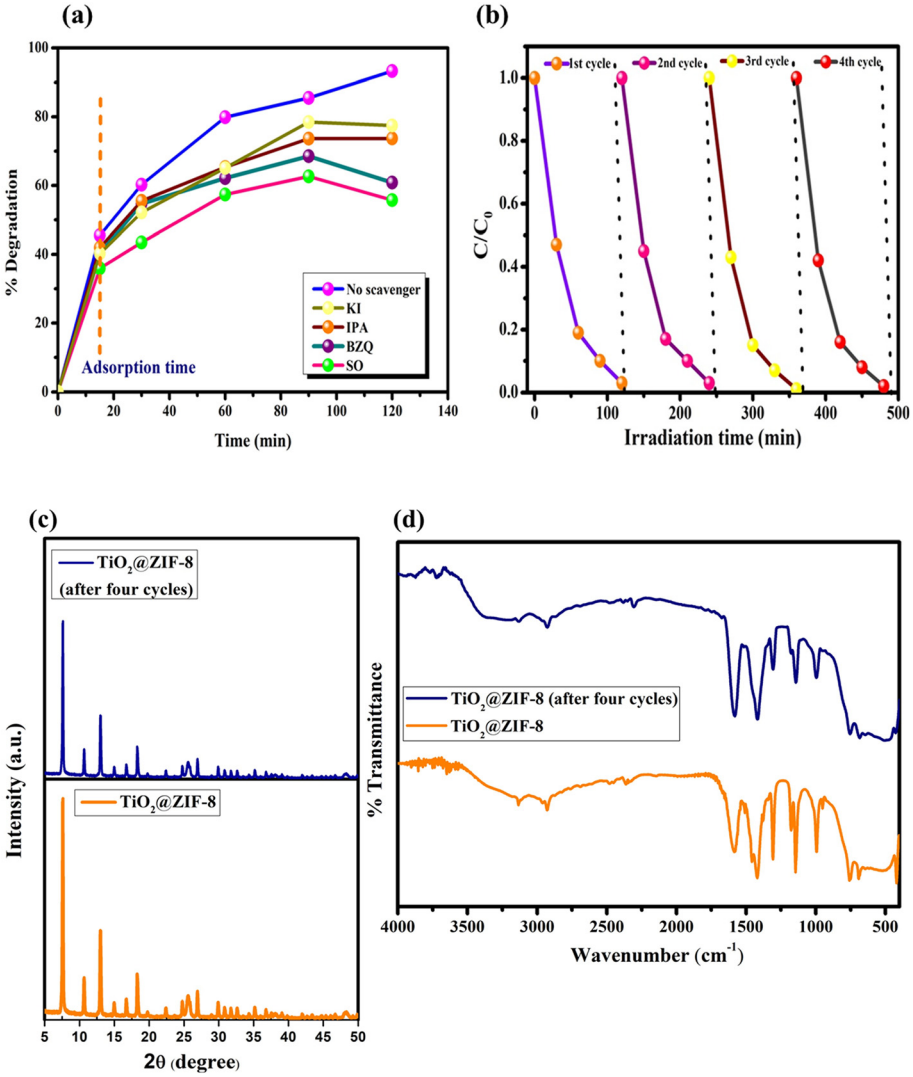

Fig. 10 (a) Effect of scavengers on CP degradation, (b) recyclability of the TiO_2@ZIF-8 catalyst for the degradation of CP, and (c) XRD pattern and (d) FTIR spectra of TiO_2@ZIF-8 before and after four cycles.

respectively.[38] The addition of these scavengers significantly reduced the degradation efficacy of the TiO_2@ZIF-8 composite from 90.2% to 58.5%, 50.9% and 50.3% after 90 min in the presence of $Na_2C_2O_4$, BQ, and IPA, respectively (Fig. 10a). These results indicated that h^+, $\cdot O_2^-$, and ·OH were crucial contributors to the degradation process. The significant decrease was obtained using IPA and BQ, emphasizing ·OH, h^+ and $\cdot O_2^-$ as the major active species, while KI confirmed that the surface ·OH radicals played a minimal role. The quantitative data presented in supplementary information Fig. S6b provide a hierarchical understanding of the reactive species, confirming their synergistic contribution to the high photocatalytic efficiency of the TiO_2@ZIF-8 composite. The obtained results supported the proposed type-II heterojunction mechanism, where effective charge separation promoted the formation of multiple reactive oxygen species (ROS), thereby enhancing the overall photocatalytic activity of the TiO_2@ZIF-8 heterostructure.

3.7 Heterogeneity and recyclability study

The heterogeneous nature of the catalyst was further examined by conducting photocatalytic degradation experiments using the filtrate obtained after the thorough washing and removing the solid catalyst. The filtrate was separated carefully to ensure the absence of residual catalyst particles, thereby eliminating any contribution from heterogeneous catalytic sites. The degradation efficiency observed in the filtrate system was approximately 30%, which closely corresponded to the extent of degradation achieved under direct photolysis conditions. This similarity strongly indicated that the contribution of dissolved or leached active species from the catalyst to the overall degradation process was negligible. Furthermore, the stability and recyclability of TiO_2@ZIF-8 were assessed over four consecutive photocatalytic cycles, as shown in Fig. 10(b), which maintained an efficiency of ~85%. The regenerated catalyst,

Open Access Article. Published on 08 April 2026. Downloaded on 6/3/2026 4:27:37 PM.
This article is licensed under a Creative Commons Attribution-NonCommercial 3.0 Unported Licence.

after four cycles of characterization by XRD and FT IR (Fig. 10(c) and (d)), revealed no significant changes in crystalline phases and vibrational signatures, indicating structural stability. These findings demonstrate that TiO_2@ZIF-8 is a highly stable and efficient photocatalyst for CP degradation.

3.8 Enhanced photocatalytic mechanism

The TiO_2@ZIF-8 nanocomposite achieved ~90% degradation of CP within 90 min under solar light. To elucidate the charge-transfer pathways, a band energy diagram was developed using Tauc plots. The VB/CB positions of ZIF-8, TiO_2, and TiO_2@ZIF-8 suggested the probable formation of a type-II heterojunction. According to the previous analysis, this could be explained based on the electronic structure and interfacial charge transfer characteristics. Under solar irradiation, TiO_2 absorbs photons and produces electron–hole pairs, while ZIF-8 facilitates interfacial electron transfer due to its more negative CB position. Mott–Schottky analysis suggests the presence of positive slopes for TiO_2 and ZIF-8, indicative of n-type semiconductors. The flat-band potentials were determined to be −0.43 and −1.31 V for TiO_2 and ZIF-8, respectively.

For n-type semiconductors, the conduction band (CB) potentials were estimated to be approximately 0.2 V more negative than the flat-band potentials, which yielded CB positions of −0.63 and −1.28 V for TiO_2 and ZIF-8, respectively. Based on their respective bandgaps (3.2 eV for TiO_2 and 4.0 eV for ZIF-8, determined from UV-vis DRS), the valence band (VB) positions were estimated as +2.57 V for TiO_2 and +2.49 V *vs.* NHE for ZIF-8. This band alignment indicated the formation of a type-II heterojunction, where photogenerated electrons transferred from the CB of ZIF-8 to that of TiO_2, while holes migrated from the VB of TiO_2 to that of ZIF-8, thereby facilitating efficient charge separation and suppressing electron–hole recombination (Fig. 11).

The VB potential of TiO_2 was positive enough to oxidize H_2O/OH^- into ·OH radicals, while the CB potential of ZIF-8 was more negative than the $O_2/{\cdot}O_2^-$ redox potential, enabling the reduction of dissolved oxygen into ${\cdot}O_2^-$ radicals. Some of the ${\cdot}O_2^-$ species further underwent proton-assisted reactions to form H_2O_2, which could decompose into additional ·OH radicals. The resulting spatial separation of charge carriers significantly reduced recombination losses and enhanced the photocatalytic efficiency, as evidenced by the improved degradation performance under solar light. The formation of this heterojunction with favorable band alignment provided a rational explanation for the observed enhancement in the photocatalytic activity of TiO_2@ZIF-8. The interfacial electric field formed at the heterojunction further accelerated this charge separation while suppressing recombination. This migration of e^- and h^+ was driven purely by the energetic gradient and the interfacial electric field at the TiO_2@ZIF-8 junction. Additionally, interfacial ligand-to-metal charge transfer (LMCT) and linker defect states in ZIF-8 help slightly extend the absorption of the composite.[39] The porous ZIF-8 framework additionally enhanced photocatalytic efficiency by (1) providing a high surface area for reactant adsorption, (2) facilitating mass transport of reactants/products, (3) suppressing electron–hole recombination due to interfacial electric fields, and (4) potentially offering molecular sieving effects.

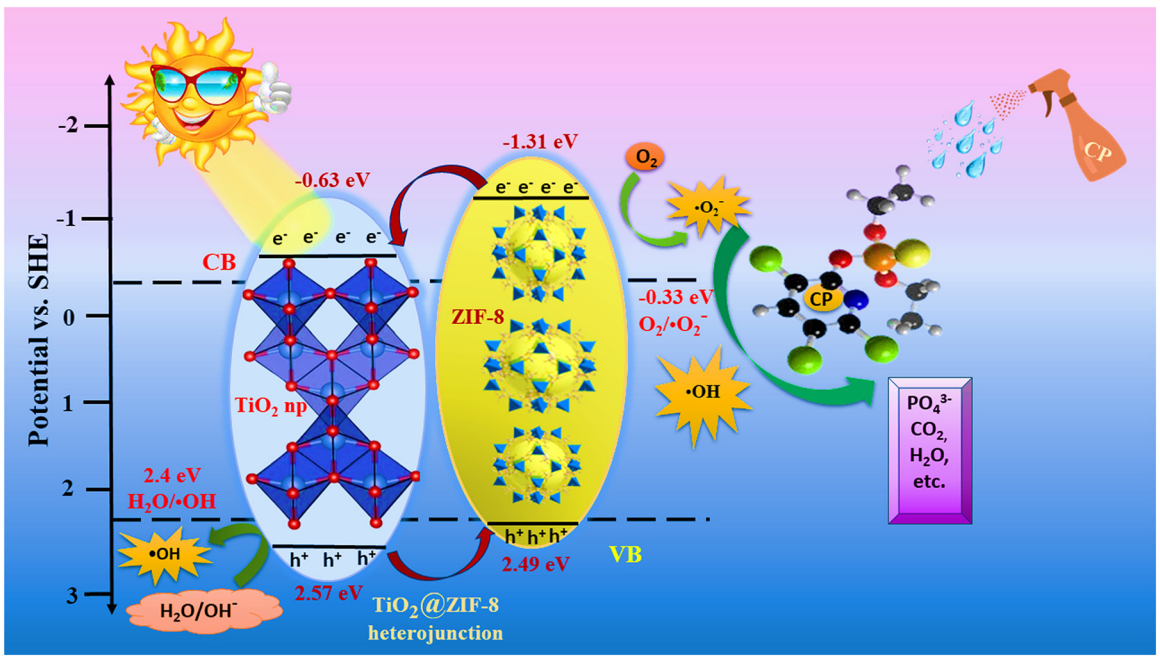

Fig. 11 Schematic presentation of photocatalytic degradation mechanism of chlorpyrifos (CP) by TiO_2@ZIF-8.

© 2026 The Author(s). Published by the Royal Society of Chemistry

Open Access Article. Published on 08 April 2026. Downloaded on 6/3/2026 4:27:37 PM. This article is licensed under a Creative Commons Attribution-NonCommercial 3.0 Unported Licence.

Under solar light, the photocatalytic degradation of CP proceeded through multiple reactive pathways. Initially, photoexcitation generated electron–hole pairs in the TiO_2@ZIF-8 heterostructure, with electrons (e^-) promoted to the conduction band (CB) while leaving holes (h^+) in the valence band (VB). The thermodynamic potentials drove subsequent redox reactions: (1) the VB potential of TiO_2 (+2.57 V *vs.* NHE) exceeded the oxidation potential of H_2O/·OH (+2.4 V *vs.* NHE), enabling h^+ to oxidize adsorbed H_2O/OH^- to generate hydroxyl radicals (·OH). (2) Simultaneously, the more negative CB potential of ZIF-8 (−1.31 V *vs.* NHE) compared to O_2/$\cdot O_2^-$ (−0.33 V *vs.* NHE) facilitated oxygen reduction by photoelectrons to produce superoxide radicals ($\cdot O_2^-$).[39] (3) These primary reactive species further interacted through secondary reactions, where some $\cdot O_2^-$ radicals combined with protons to form additional ·OH.

$$TiO_2@ZIF\text{-}8 + h\nu \rightarrow TiO_2@ZIF\text{-}8 + (h^+_{VB}, e^-_{CB}) \text{ pairs},$$

$$H_2O/(OH^-) + TiO_2\ (h^+) \rightarrow \cdot OH + H^+,$$

$$O_2 + ZIF\text{-}8\ (e^-) \rightarrow \cdot O_2^-,$$

$$\cdot O_2^- + TiO_2\ (h^+) + \cdot OH + CP \rightarrow PO_4^{3-} + CO_2 + H_2O + \text{small molecules}.$$

3.9 Probable degradation pathway

GC-MS analysis confirmed the stepwise degradation of chlorpyrifos (CP, m/z = 350) into several intermediates, followed by mineralization, as presented in Fig. 12 and 13. The first step involved oxidative dealkylation, yielding demethylated derivatives F1 and F2 (m/z = 336), followed by the hydrolytic cleavage of the P–O–aryl bond to form F3 (m/z = 294). Again, the hydrolysis of the phosphorothioate group of CP into F4 (m/z = 196), identified as 3,5,6-trichloro-2-pyridinol (TCP), was observed. TCP underwent dechlorination and ring-cleavage, resulting in F6 (m/z = 180), while the parallel degradation of the thiophosphoryl group produced phosphorothioate derivatives F5 (m/z = 170), F7 (m/z = 113), F8, and F9 (m/z = 127) through sequential dealkylation, desulfuration, and oxidation. The disappearance of CP and its intermediates, along with the formation of CO_2, H_2O, PO_4^{3-}, and NH_3 at the m/z values of 44, 18, 97 and 16, respectively, indicated complete mineralization. Overall, the results suggested that the degradation process involved hydrolysis, oxidative dealkylation, dechlorination, and ring cleavage, demonstrating an efficient pathway for the detoxification and mineralization of chlorpyrifos.

3.10 Anti-microbial analysis

The antibacterial activity of the TiO_2@ZIF-8 nanocomposite was evaluated by measuring the inhibition zones on agar plates against both *E. coli* and *S. aureus* (Fig. S9). The TiO_2@ZIF-8 (10 μg mL^{-1}) nanocomposite exhibited significant antibacterial activities compared to other dosages. The positive control exhibited a prominent zone of inhibition, confirming the reliability of the assay, whereas the negative control showed no visible inhibition, validating the absence of any background antibacterial effect. In the case of *E. coli*, the TiO_2@ZIF-8 (10 μg mL^{-1}) nanocomposite demonstrated a distinct inhibition zone of approximately 14–15 mm, indicating significant antibacterial activities. While for *S. aureus*, the inhibition zone diameters were found to be 4–6 mm, which was less than the positive control but clearly active compared to the negative control. This is because the partial degradation of the ZIF-8 framework in biological media releases Zn^{2+} ions, which readily penetrate the thin Gram-negative outer membrane of *E. coli*, disrupt essential enzymes, and induce metabolic toxicity. Simultaneously, direct contact between bacterial cells and the high-surface-area composite promoted membrane disruption through exposure to surface metal nodes, and chelation enhanced penetration. Under light irradiation, TiO_2 generated reactive oxygen species (·OH, $\cdot O_2^-$, h^+) that oxidatively damaged lipids, proteins, and nucleic acids, and those ROS diffuse more easily through the less-rigid Gram-negative cell envelope,

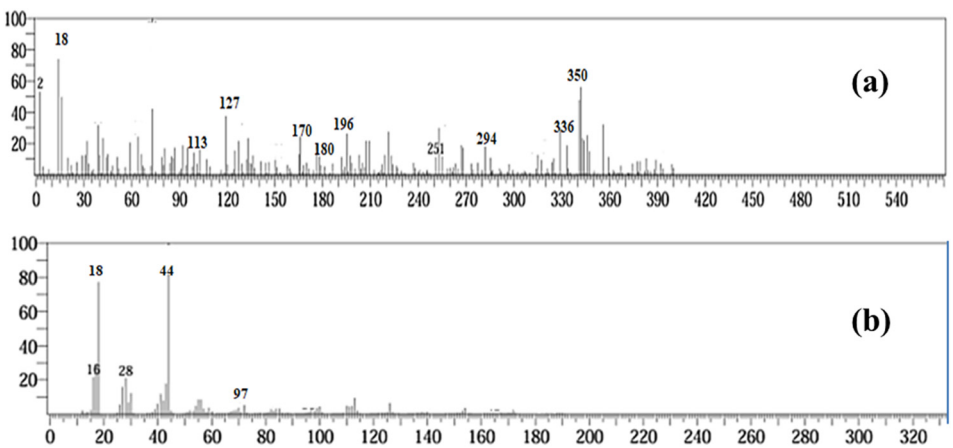

Fig. 12 Fragments of CP (a) after the commencement of the reaction and (b) after the completion of the reaction.

Open Access Article. Published on 08 April 2026. Downloaded on 6/3/2026 4:27:37 PM.
This article is licensed under a Creative Commons Attribution-NonCommercial 3.0 Unported Licence.

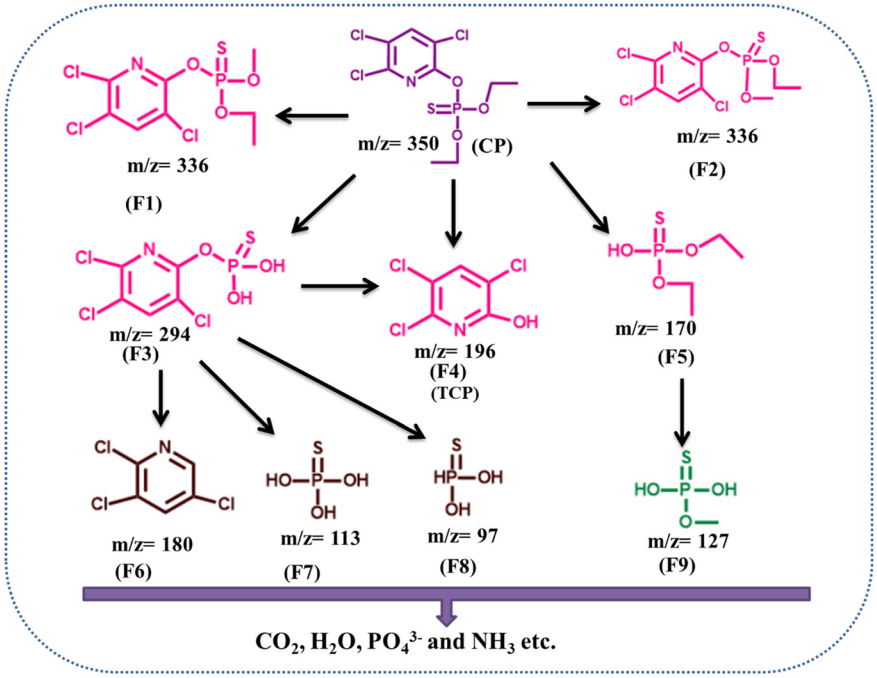

Fig. 13 Degradation pathway of CP by TiO_2@ZIF-8.

while the thick peptidoglycan layer of *S. aureus* offered partial protection. Additionally, ligand-exchange interactions (HSAB effect) could accelerate Zn^{2+} release and generate more reactive surface sites.[40] Further, the incorporation of TiO_2 into the porous ZIF-8 framework provided a high surface area, improved dispersion, and enhanced light-harvesting capability, which together promoted high ROS generation.[41,42] Together, Zn^{2+} ion toxicity, contact-mediated membrane disruption, ROS-induced oxidative stress, and linker-exchange degradation synergistically accounted for the high susceptibility of *E. coli*.[42] These findings highlight TiO_2@ZIF-8 as a potential candidate for antimicrobial applications, with potential utility in water disinfection, biomedical coatings, and environmental remediation.

4. Conclusion

TiO_2@ZIF-8 heterostructures were successfully fabricated *via* hydrothermal and ultrasonication methods, and they showed significant photocatalytic and antimicrobial performance. TiO_2@ZIF-8 heterostructures achieved the efficient photocatalytic degradation of CP at 90.9% with 100 mg L^{-1} of CP, using 30 mg of a catalyst within 90 min under solar light, and they exhibited better homogeneity and stability, maintaining activity even after four successive cycles. The superior photocatalytic efficiency of TiO_2@ZIF-8 was attributed to its type-II heterojunction structure, which promoted charge carrier dynamics and broadened visible-light utilization. Radical quenching studies confirmed $O_2^{\cdot-}$, h^+, and ·OH as the major species in CP degradation. Additionally, the composite demonstrated notable antibacterial efficacy against *E. coli* and *S. aureus*, establishing its promise as a multifunctional material for environmental remediation.

Author contributions

Sushanta Kumar Badamali is responsible for supervision, formal analysis, and resources. Subhashree Mohanty is responsible for writing – review and editing, writing – original draft, methodology, investigation, formal analysis, data curation, and software, and Bibeka Nanda Marai is responsible for methodology.

Conflicts of interest

Authors declare no conflicts of interest.

Data availability

Data will be made available by the authors upon request.

Supplementary information (SI) is available. See DOI: https://doi.org/10.1039/d5lf00405e.

Acknowledgements

The authors acknowledge the Government of Odisha, India, for the award of the MRIP fellowship. We acknowledge the support of JNCASR, Bangalore, and the Material Analysis and Research Center, Karnataka, for XRD measurement and BET analysis. We are also thankful to CRF, KIIT, Bhubaneswar and, IIT Hyderabad for[34] FE SEM and, XPS analysis, respectively.

© 2026 The Author(s). Published by the Royal Society of Chemistry

Open Access Article. Published on 08 April 2026. Downloaded on 6/3/2026 4:27:37 PM. This article is licensed under a Creative Commons Attribution-NonCommercial 3.0 Unported Licence.

References

1 F. H. Tang, M. Lenzen, A. McBratney and F. Maggi, *Nat. Geosci.*, 2021, **14**, 206–210.
2 E. M. John and J. M. Shaike, *Environ. Chem. Lett.*, 2015, **13**, 269–291.
3 F. H. Tang, M. Lenzen, A. McBratney and F. Maggi, *Nat. Geosci.*, 2021, **14**, 206–210.
4 E. Wołejko, B. Łozowicka, A. Jabłońska-Trypuć, M. Pietruszyńska and U. Wydro, *Int. J. Environ. Res. Public Health*, 2022, **19**, 12209.
5 K. Jamil, A. P. Shaik, M. Mahboob and D. Krishna, *Drug Chem. Toxicol.*, 2005, **28**, 447–459.
6 K. Piaskowski, R. Świderska-Dąbrowska and P. K. Zarzycki, *J. AOAC Int.*, 2018, **101**, 1371–1384.
7 D. S. Bhatkhande, V. G. Pangarkar and A. A. C. M. Beenackers, *J. Chem. Technol. Biotechnol.*, 2002, **77**, 102–116.
8 X. Wei, G. Zhu, J. Fang and J. Chen, *Int. J. Photoenergy*, 2013, **2013**, 726872.
9 L. Ren, Y. Li, M. Mao, L. Lan, X. Lao and X. Zhao, *Appl. Surf. Sci.*, 2019, **490**, 283–292.
10 H. Dai, X. Yuan, L. Jiang, H. Wang, J. Zhang and T. Xiong, *Coord. Chem. Rev.*, 2021, 441.
11 Y. H. Zou, H. N. Wang, X. Meng, H. X. Sun and Z. Y. Zhou, *Nanoscale Adv.*, 2021, **3**, 1455–1463.
12 A. N. Ökte and D. Tuncel, *Photochem. Photobiol. Sci.*, 2025, 1–20.
13 W. Wang, C. Shen, R. Shao, Y. Zhu, W. Yu, X. Wu and Z. Xu, *et al.*, *Colloids Surf., A*, 2025, **714**, 136568.
14 F. Zisti, F. J. M. Al-Behadili, M. Nadimpour, R. Rahimpoor, N. Mengelizadeh, A. Alsalamy and D. Balarak, *Environ. Res.*, 2024, **245**, 118019.
15 H. Teymourinia, H. A. Alshamsi, A. Al-Nayili and M. Gholami, *Chemosphere*, 2023, **344**, 140325.
16 Y. Tian, Q. Liu, S. Lin, X. Liang, S. Khan, X. Yang and X. Wang, *J. Environ. Chem. Eng.*, 2023, **11**, 110054.
17 X. Liu, Z. H. Peng, L. Lei, R. X. Bi, C. R. Zhang, Q. X. Luo and J. D. Qiu, *Appl. Catal., B*, 2024, **342**, 123460.
18 Y. Pan, Y. Liu, G. Zeng, L. Zhao and Z. Lai, *Chem. Commun.*, 2011, **47**, 2071–2073.
19 Z. Ma, B. Guan, J. Guo, Y. Chen, J. Chen, H. Dang and Z. Huang, *Ind. Eng. Chem. Res.*, 2023, **62**, 17658–17670.
20 R. Li, W. Li, C. Jin, Q. He and Y. Wang, *J. Alloys Compd.*, 2020, **825**, 154008.
21 K. Zhou, B. Mousavi, Z. Luo, S. Phatanasri, S. Chaemchuen and F. Verpoort, *J. Mater. Chem. A*, 2017, **5**, 952–957.
22 M. R. Barik and S. K. Badamali, *ChemistrySelect*, 2025, **10**, e01792.
23 A. Semwal, D. Sajwan, J. Rawat, L. Gambhir, H. Sharma and C. Dwivedi, *Environ. Sci. Pollut. Res.*, 2023, **30**, 45827–45839.
24 G. Kumari, K. Jayaramulu, T. K. Maji and C. Narayana, *J. Phys. Chem. A*, 2013, **117**, 11006–11012.
25 L. Cen, T. Tang, F. Yu, H. Wu, C. Li, H. Zhu and Y. Guo, *J. Ind. Eng. Chem.*, 2023, **126**, 537–545.
26 L. Bogdan, A. Palcic, M. Duplancic, M. Leskovac and V. Tomašic, *Processes*, 2023, **11**, 1234.
27 S. Angela, V. B. Lunardi, K. Kusuma, F. E. Soetaredjo, J. N. Putro, S. P. Santoso and S. Ismadji, *Environ. Nanotechnol., Monit. Manage.*, 2021, **16**, 100598.
28 Z. Ma, B. Guan, J. Guo, Y. Chen, J. Chen, H. Dang and Z. Huang, *Ind. Eng. Chem. Res.*, 2023, **62**, 17658–17670.
29 J. A. Thompson, K. W. Chapman, W. J. Koros, C. W. Jones and S. Nair, *Microporous Mesoporous Mater.*, 2012, **158**, 292–299.
30 C. Muthukumar, E. Iype, K. Raju, S. Pulletikurthi and B. P. Kumar, *J. Mol. Struct.*, 2022, **1263**, 133194.
31 E. M. Hotze, T. Phenrat and G. V. Lowry, *J. Environ. Qual.*, 2010, **39**, 1909–1924.
32 S. H. Khan, B. Pathak and M. H. Fulekar, *Nanotechnol. Environ. Eng.*, 2018, **3**, 13.
33 M. Mohammadi, S. Sabbaghi, M. Binazadeh, S. Ghaedi and H. Rajabi, *Chemosphere*, 2023, **336**, 139311.
34 M. S. Mohtaram, S. Sabbaghi, J. Rasouli and K. Rasouli, *Environ. Pollut.*, 2024, **347**, 123746.
35 A. M. Dugandžić, A. V. Tomašević, M. M. Radišić, N. Ž. Šekuljica, D. Ž. Mijin and S. D. Petrović, *J. Photochem. Photobiol., A*, 2017, **336**, 146–155.
36 J. Zhang, X. Gao, W. Guo, Z. Wu, Y. Yin and Z. Li, *RSC Adv.*, 2022, **12**, 6676–6682.
37 C. Mohanty, A. Samal, A. K. Behera and N. Das, *J. Water Process Eng.*, 2024, **65**, 105821.
38 Y. Wang, Q. Wang, X. Zhan, F. Wang, M. Safdar and J. He, *Nanoscale*, 2013, **5**, 8326–8339.
39 S. Navalon, A. Dhakshinamoorthy, M. Alvaro, B. Ferrer and H. Garcia, *Chem. Rev.*, 2022, **123**, 445–490.
40 R. K. Alavijeh, S. Beheshti, K. Akhbari and A. Morsali, *Polyhedron*, 2018, **156**, 257–278.
41 J. Cui, D. Wu, Z. Li, G. Zhao, J. Wang, L. Wang and B. Niu, *Ceram. Int.*, 2021, **47**, 15759–15770.
42 S. Sadiq, I. Khan, M. Humayun, P. Wu, A. Khan and M. Bououdina, *ACS Omega*, 2023, **8**(51), 49244–49258.

© 2026 The Author(s). Published by the Royal Society of Chemistry